Acta Materialia 103 (2016) 893–908

Contents lists available at ScienceDirect

Acta Materialia

journal homepage: www.elsevier.com/locate/actamat

Full length article

Intergranular damage during stress relaxation in AISI 316L-type austenitic stainless steels: Effect of carbon, nitrogen and phosphorus contents

H. Pommier [a], E.P. Busso [a, b, *], T.F. Morgeneyer [a], A. Pineau [a]

[a] MINES ParisTech, Centre des matériaux, CNRS UMR 7633, BP 87, 91003, Évry, France
[b] Scientific Directorate, ONERA, BP 80100, 91123, Palaiseau, France

ARTICLE INFO

Article history:
Received 25 May 2015
Received in revised form
23 October 2015
Accepted 3 November 2015
Available online xxx

Keywords:
Reheat cracking
AISI 316L austenitic stainless steel
Intergranular damage
Stress relaxation
Synchrotron tomography

ABSTRACT

This work concerns a study of the mechanisms responsible for intergranular cracking during high temperature stress relaxation in AISI 316L-type austenitic stainless steels. This phenomenon, also known as reheat cracking, is typically present in heat affected zones of massive welded parts used in the energy industry. Here, five steel grades with different C, N and P contents were considered to assess the effects of chemical composition on the three main mechanisms potentially responsible for reheat cracking, namely intergranular $M_{23}C_6$ carbide precipitation, stress relaxation phenomena, and intergranular P segregation. After testing the five AISI 316L-type grades under reheat cracking conditions by a pre-compressed CT-like specimen technique, different degrees of intergranular damage were observed in the specimens by optical microscopy and synchrotron X-ray tomography. Detailed grain boundary analyses by SEM and TEM in the five different steel grades showed the main mechanism responsible for reheat cracking to be the nucleation of microcavities at intergranular $M_{23}C_6$ carbides in high residual stress regions. The addition of P was found to increase the number of cavitated GBs but not to be the dominant mechanism responsible for intergranular damage. A comparison between elasto-plastic finite element predictions of the residual stresses in the CT-specimens and the results of microstructural investigations revealed no intergranular damage in regions where the initial maximum principal stresses in the specimens were below 740 ± 30 MPa.

1. Introduction

Reheat cracking (RC), also known as stress relaxation or stress relief cracking, is an intergranular damage phenomenon found in heat affected zones (HAZ) of thick welded parts (*e.g.* steam header/nozzle in Advanced Gas Cooled Reactors [1]). Some of the materials which exhibit such mode of failure are austenitic stainless steels reheated at high temperatures (773–973 K) during either post-weld heat treatment or service. Such intergranular damage is known to be driven by the high temperature relaxation of residual stress fields initially introduced during the welding process due to thermal strain incompatibilities. These incompatibilities depend on the weld configuration and on the component thickness, as industrial RC cases are typically known to occur near attachment welds where the cross-sectional thickness is above 30–40 mm. The main objective of this work is to investigate the effects of C, N and P contents on RC damage development in AISI 316L-type austenitic stainless steels. In the mid-fifties, the first industrial cases of RC were described and studied on stabilised austenitic stainless steels[1] [2–5]. Massive welded pipes of 347 and 321 steel grades (Nb and Ti-stabilised austenitic stainless steels, respectively) were found to be prone to RC during high temperature service. 304-type and 316-type non-stabilised austenitic stainless steels, which do not exhibit intragranular precipitation of Ti or Nb-carbides, were found to be less sensitive to RC [6], but not immune to, as this phenomenon was observed in 304H [7,8] and 316H [1,9]. More recently, 316L and

* Corresponding author. Scientific Directorate, ONERA, BP 80100, 91123, Palaiseau, France.
E-mail addresses: harry.pommier@ensmp.fr (H. Pommier), esteban.busso@onera.fr (E.P. Busso), thilo.morgeneyer@ensmp.fr (T.F. Morgeneyer), andre.pineau@ensmp.fr (A. Pineau).

[1] Thereafter, the AISI numbering system is implicitly assumed when designating 300 series steels.

http://dx.doi.org/10.1016/j.actamat.2015.11.004

316L(N) steels [10,11] were found to be sensitive to intergranular cracking under reheat cracking conditions. However, as far as the authors are aware, no evidence of in-service RC has been reported in 316L-type steels.

The main mechanical condition for RC to occur was found to be the presence of high tensile residual stress fields in the material before thermal exposure at high temperatures. During the welding process of massive parts, thermal strain incompatibilities induce the formation of predeformed zones and the development of residual stress fields near the weld. The level of residual stresses required to develop RC in annealed austenitic stainless steels was found to be only attainable by strain hardening [11,12]. Besides, high stress triaxialities were also found to increase RC damage [13]. Those observations are consistent with the lower creep ductility observed in austenitic stainless steels on predeformed states [10,14–16] and subjected to high stress triaxialities [13,17].

Several mechanisms were suggested to explain the RC susceptibility of predeformed austenitic stainless steels. In 347 and 321 steels, it was first attributed to strain-induced precipitation hardening due to Nb(C,N) and Ti(C,N) carbides [5,18–20]. However, Chabaud-Reytier *et al.* [12] suggested that intragranular Ti(C,N) carbide precipitation was not the predominant mechanism responsible for RC in 321 steel. Instead, they attributed this mode of failure to solute solid solution atoms (C and N) which impede the mobility of dislocations and thus reduce the residual stress relaxation rate. Those solid solution atoms can explain the susceptibility of non-stabilised austenitic stainless steels to RC, and also suggest that the grades with high solute atom contents would be more sensitive than low content ones. This understanding was not confirmed by the observations of Auzoux *et al.* [11] on 316H, 316L(N) and 316L steels exposed to RC conditions. They found that the global content of solute atoms cannot explain the various sensitivities of 316-type grades to RC since the tested 316L (low C and low N) was found to be the most prone to RC. Thus, the respective effects of C and N contents in solid solution are still unclear.

Another mechanism known to be responsible for intergranular damage in austenitic stainless steel is intergranular carbide precipitation. During service at temperatures close to 823 K, grain boundary (GB) strength can be impaired by the precipitation of intergranular carbides (mostly, Fe(Cr,Mo)-rich $M_{23}C_6$) which is accelerated by prior room-temperature (RT) deformation [21]. More recently, Hong *et al.* [22] and Jones *et al.* [23] investigated the relationship between GB characteristics and the formation of intergranular $M_{23}C_6$ carbides in austenitic stainless steels. They concluded that the presence of $M_{23}C_6$ depends on GB type: highly random misoriented GBs exhibit more carbide precipitation than $\Sigma3$ boundaries. Besides, the shape of intergranular carbides is linked to GB characteristics: as misorientation between adjacent grains increases, the carbide morphology tends to change from plate-like to acute triangular shapes. The latter $M_{23}C_6$ carbide morphology can explain the more pronounced cavitation observed on random highly misoriented GBs during creep at high temperature [22,24,25].

A third mechanism which can potentially affect the cohesive strength of GBs, and hence RC, is the intergranular segregation of impurities such as S and P [26]. In comparison with P, intergranular S segregation is less important in austenitic stainless steels [27] due to the formation of non-metallic MnS inclusions during hot-rolling. Sulphur is thus unlikely to affect creep cavitation in 316L-type austenitic stainless steels. Similarly to intergranular carbide precipitation, GB misorientations can also affect intergranular segregation levels. For instance, it was observed that $\Sigma3$ GBs present less P segregation than other types in Fe-Cr-Ni [28] and Fe–Mn–C steels [29].

The mechanisms of intergranular $M_{23}C_6$ carbide precipitation and P segregation can affect each other. Kegg *et al.* [30] showed that P segregation accelerates both the nucleation and growth rate of $M_{23}C_6$ carbides. Their propensity to reduce GB strength was reported by Chen *et al.* [31]. At 77 K, the intergranular fracture surface of 316H austenitic stainless steel was found to be an increasing function of intergranular $M_{23}C_6$ carbide coverage and intergranular P content. Even if a correlation exists, the relative effects of $M_{23}C_6$ carbide precipitation and P segregation on GB strength is still unclear.

The above literature review shows that RC occurs during the relaxation at high temperatures of the high tensile residual stresses initially introduced during plastic deformation of the material. However, the dominant micromechanisms responsible for grain boundary weakening at high temperatures are still not fully understood. This includes the role of $M_{23}C_6$ carbide precipitation, the effects of C and especially N contents on stress relaxation kinetics, as well as the effect of intergranular P segregation.

Several published works have dealt with the development of experimental methods to reproduce stress relaxation cracking at the laboratory scale [32–36]. The procedure developed by Turski *et al.* [37], which consists of introducing a triaxial tensile residual stress field at the notch root of a CT-like specimen by pre-compression at RT, enables the magnitude of the maximum residual stress in the notch root region to be controlled. This approach also makes it possible for stress relaxation cracking of homogeneous microstructures to be studied under known residual stress fields. The method to be used in this work is based on this pre-compressed CT technique.

The paper is structured as follows. First, three industrial steel grades (various C and N contents, similar P contents) and two laboratory-made grades (similar C and N contents, one with high P, another with very low P) are described. Then, the RC experimental procedure of pre-compressed CT-like specimen is explained. Afterwards, the mechanical response of the materials at room and high temperatures is investigated, characterised and modelled to predict the residual stress and strain fields in the CT specimens. The results of RC experiments, conducted on the five 316L-type grades, are next presented. In this part, the resulting intergranular damage is quantitatively studied using optical and scanning electron microscopy (OM and SEM), electron back scatter diffraction (EBSD), transmission electron microscopy (TEM) and local X-ray synchrotron tomography techniques. Finally, the effects of temperature, C, N and P on RC damage development are discussed. The resulting conclusions are then used to explain the different resistances of the five 316L-type steel to RC.

2. Materials and experimental procedures

2.1. Materials

The chemical compositions of the five 316L-type austenitic

Table 1
Chemical compositions of the AISI 316L-type steels (wt.%).

	IA	IB	IC	HP	LP
C	0.033	0.028	0.011	0.014	0.014
N	0.025	0.077	0.068	0.081	0.066
P	0.022	0.023	0.028	0.052	0.001
Cr	←		16.4–17.4		→
Ni	←		11.0–13.6		→
Mo	←		2.0–2.6		→
Mn	←		0.8–2.1		→
S	←		0.001–0.022		→
B	←		0.001–0.002		→
Fe	←		bal.		→

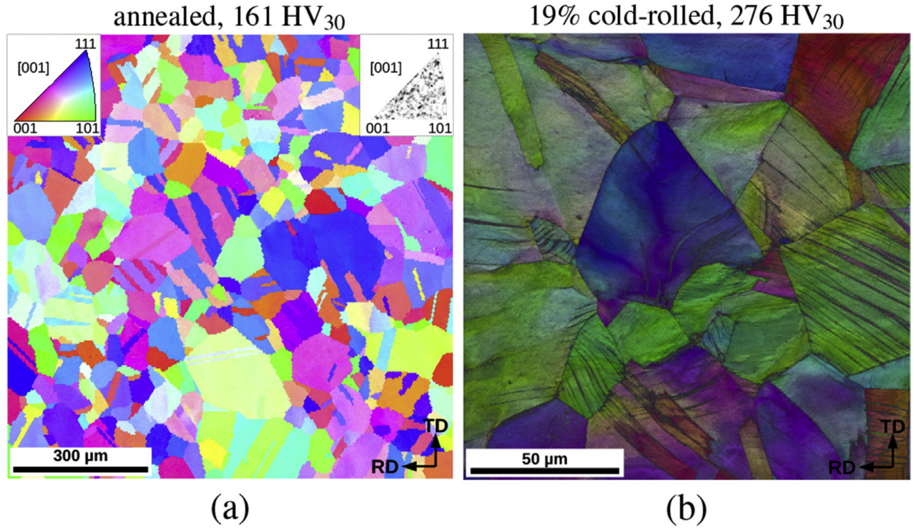

Fig. 1. Microstructure of the IB steel grade observed by EBSD: (a) annealed state shown in an inverse pole figure (IPF) and (b) cold-rolled state, in a close-up view, shown by a superposition of the IPF and image quality maps.

stainless steels are given in Table 1. Here, IA, IB and IC are designations of industrial grades that were received in annealed states (respectively at 1373, 1323 and 1373 K, for 30, 30 and 90 min before being water quenched), in the form of 14, 40 and 33 mm-thick sheets. Laboratory-made high P (HP) and low P (LP) steels were specially cast for this study by Ugitech and hot-rolled at 1385 ± 15 K into 30 mm-thick sheets by OCAS. Upon receipt, they were annealed at 1373 K for 10 min and water quenched to obtain a grain size similar to that of industrial grades. The grain size of the five steel grades was found to be 40 ± 6 μm. The five annealed microstructures were composed of equiaxed austenitic grains containing annealing twins and showed no crystallographic texture. A microstructure representative of the five steel grades in the annealed state is shown in Fig. 1(a) (RD and TD stand for, respectively, (hot-)rolling and transverse directions). MnS intragranular inclusions, which are aligned and elongated along the RD, were observed in all grades, especially in IA which has a higher S content. Their chemical compositions were confirmed by energy-dispersive X-ray spectroscopy (EDS).

The annealed plates were then cold-rolled in the same direction as the original hot-rolling one to reduce their thickness by 20 ± 2%. For the five grades, Vicker's hardness increased from 135–208 HV_{30} in the annealed state to 274–282 HV_{30} in the cold-rolled state. The latter hardness values are higher than the maximum value of 230 HV_{30} measured by Auzoux [38] in the most highly deformed zone of a multi-pass weld. Therefore, the use of this five cold-rolled materials for the RC studies should enable the residual stress fields to be introduced to be greater than the ones found in industrial parts. It should be noted that the microstructure of the five cold-rolled materials is different than the one observed in industrial RC-affected zones since deformation twins were observed (see Fig. 1(b)). The absence of deformation twins in industrial RC-affected zones is due to the higher temperature of deformation (~ 923 K [38]) during welding. Furthermore, SEM observations of the cold-rolled materials revealed no grain boundary damage (*e.g.* microcavities), at least whithin the peak resolution of the SEM used in this work[2].

2.2. *Reheat cracking reproduction procedure*

Reheat cracking was reproduced at a laboratory scale using CT-like specimens cut by wire-EDM from the cold-rolled plates (see geometries in Fig. 2(a)). Two CT specimen thicknesses (e = 10 and 20 mm) were used depending on the available plate thickness. To study the effect of mechanical conditions on RC damage development, three notch radii (r = 0.5, 1 and 2 mm) were tested for the IB grade steel. In Fig. 2, the notch plane (XZ) is normal to the RD (Y-direction) to maximise the residual stresses to be introduced in the specimens. The specimen thickness and notch radius values are given in Table 2. In this work, the residual stress fields in the CT-like specimens were introduced by mechanical loading rather than by the thermal strain incompatibilities associated with the welding of actual thick industrial components. Here, the replication of typical component thicknesses was not assumed to be necessary to obtain the required level of residual stresses since high residual stress levels are obtained by mechanical loading. Furthermore, the CT specimen thicknesses (10–20 mm) remain large in comparison to early reheat crack sizes (*i.e.* of the order of the grain size [37]).

The RC reproduction procedure consists of two steps:

(i) Residual stress introduction

Residual stresses were introduced in CT-like specimens by RT compression along the Y-direction (RD, see Fig. 2(a)) using geometrically-adapted cylindrical-headed fixtures and a 100 kN servo-hydraulic testing machine. Compressing forces of 25 and 50 kN were applied to the 10 and 20 mm-thick CT specimens, respectively. Thus, a confined plastically deformed zone was introduced in the notch root region. Upon unloading, the self-equilibrating elastic strains in the specimen led to the formation of a tensile residual stress field in the plastically deformed zone.

(ii) Residual stress relaxation at high temperature

Afterwards, the CT specimens were thermally exposed to constant temperatures of either 823, 848 or 873 K in resistance furnaces for 500–4313 hrs (about 1–6 months). The specimens were then removed from the furnace and air-cooled to RT. The testing conditions of each CT specimen are given in Table 2.

[2] FEI Nova NanoSEM 450 S-FEG SEM.

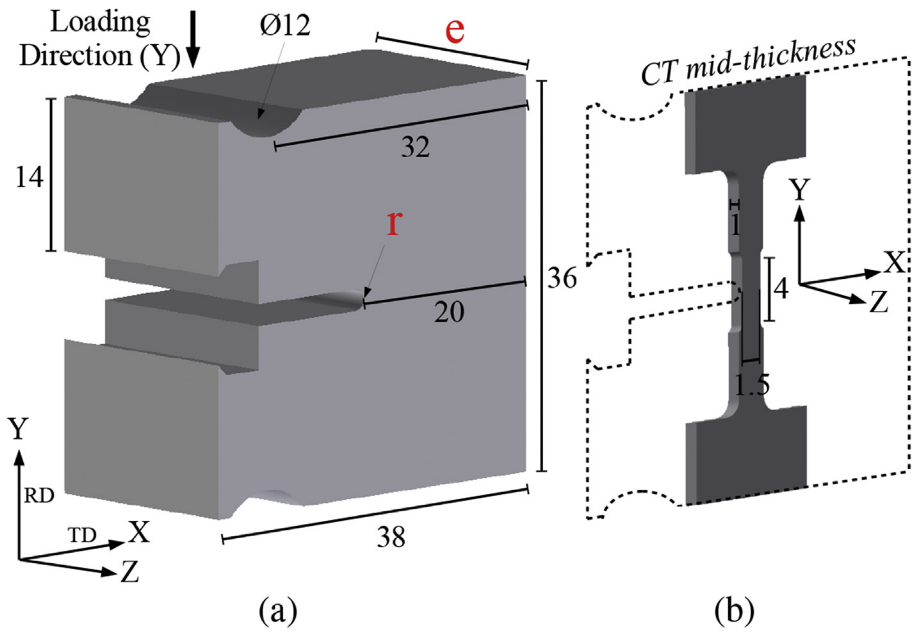

Fig. 2. (a) CT-like specimen geometries in mm, e ∈{10,20} and r ∈{0.5,1,2} (see Table 2) and (b) *in situ* tensile specimen machined from the CT specimen mid-thickness for SEM and synchrotron tomography studies.

2.3. Microstructural characterisation techniques

After their thermal exposures, the CT specimens were cut through their mid-thicknesses (XY plane) by wire-EDM. One of the resulting mid-thickness surfaces was polished and analysed by optical microscopy, SEM and EBSD. A FEI Nova NanoSEM 450 microscope (field emission gun) coupled with an EDAX TSL Hikari camera running with OIM system was used for EBSD data acquisition. The acceleration voltage was 20 kV, the working distance was close to 14 mm and the step size was 100 nm following an hexagonal grid. In order to reveal intergranular microcavities or microcracks while minimising the risk of dislocating grain boundary carbides, mechanical polishing with grinding papers (from 40 to 3 μm) and diamond pastes (from 3 to 1 μm) was performed, followed by a light etching with a solution of colloidal silica during 5 min.

The remaining half specimen was used to machine tensile specimens for either *in situ* synchrotron X-ray tomography or *in situ* SEM observations. Their geometry and the area from which they were machined are shown in Fig. 2(b). The tensile specimens from IA and IC grades were monotonically deformed *in situ* in a SEM chamber along the Y-direction by 10 ± 1% true strain. They were then 3D scanned by synchrotron X-ray tomography at the European Synchrotron Radiation Facility (ESRF, line ID15a). The scanned total volume was 1550 × 1750 × 1000 μm^3, and it was subsequently reconstructed from 2000 projections. The acquisition of projected images was performed with a filtered white beam (centered around a 60 keV X-ray energy). Tensile specimens from IB, HP and LP grades were incrementally deformed *in situ* at the ESRF with a tensile testing device specially designed for local tomography [39]. The tensile specimens were incrementally deformed from 0 to 20 ± 3% true strain along the Y-direction while performing a 3D tomography scan at each strain step. The deformation along the Y-direction was carried out to open up any existing microcavities and microcracks by plastic deformation. When the size of a defect exceeded the tomography voxel size (*i.e.* for this experiment, 1.095 μm), the defect could be detected.

To identify the chemical composition and structure of the intergranular carbides present in the CT specimens after thermal exposures, TEM observations were performed on a thin disc-shaped section machined from the IB grade specimen tested at 848 K for 3621 h (e = 20 mm, r = 1 mm). The sample was cut by wire-EDM out of the former tensile residual stress region so that early stage of intergranular damage development (*i.e.* nanocavities) could possibly be observed.

3. Mechanical analyses

3.1. Cold-rolled material responses

The mechanical responses of the five cold-rolled materials were obtained by an up to 5% compressive true strain followed by a 10% tensile deformation to describe the loading path experienced by the region ahead of the notch of CT specimens when compressed and then unloaded. Those tests where performed on axisymmetric specimens with a round section of 8 mm diameter and machined along the RD. A 100 kN servo-hydraulic machine was used and a strain rate of 10^{-3} s^{-1} was applied during the tests. Fig. 3 shows that the mechanical responses of the five cold-rolled materials at RT are similar.

3.2. Prediction of CT specimen residual stress and strain fields

Finite element simulations were carried out using the commercial Z-set software [40] to predict the residual stress and strain fields in the CT specimens. The constitutive model used to describe the mechanical behaviour of 316L-type steels, implemented into the Z-set code as a user-defined material subroutine, relies on internal variables associated with evolving microstructural length scales (*i.e.* mean dislocation and twin spacings) and a tensorial back stress. The main functional form of the viscoplastic constitutive model's flow and evolutionary relations are presented next. For the full formulation, refer to reference [41].

The finite strain hypo-elastic formulation is expressed in terms of the Jaumann rate of the Kirchhoff stress tensor as:

Table 2
CT specimen thermal exposure conditions and corresponding intergranular damage observed.

Temperature [K]	Time [h] ~580	~1470	2946	3621	4313
873	**IB_1^{20}** LP_1^{20} HP_1^{20} IA_1^{10} IC_1^{10}	**IB_1^{20}** LP_1^{20} $^{PA}\mathrm{LP}_1^{20}$ HP_1^{20} **$^{PA}\mathrm{HP}_1^{20}$**		**IB_1^{20}** LP_1^{20} HP_1^{20}	
848	**IB_1^{20}** LP_1^{20} HP_1^{20}	**IB_1^{20} IB_1^{10}** LP_1^{20} HP_1^{20} **IA_1^{10}** IC_1^{10}		**IB_1^{20} IB_2^{20} $\mathrm{IB}_{0.5}^{20}$** LP_1^{20} HP_1^{20}	
823	IB_1^{20} LP_1^{20} HP_1^{20}	IB_1^{20} LP_1^{20} $^{PA}\mathrm{LP}_1^{20}$ HP_1^{20} **$^{PA}\mathrm{HP}_1^{20}$** IA_1^{10} IC_1^{10}	**IA_1^{10}** IC_1^{10}	**IB_1^{20} IB_1^{10}** LP_1^{20} HP_1^{20}	**IA_1^{10}** IC_1^{10}

· Specimen notation: $^{pre-aged \rightarrow PA}_{steel\ grade \nearrow}\mathrm{IB}^{20 \leftarrow e\,[mm]}_{1 \leftarrow r\,[mm]}$

·Bold and red: damaged specimens

· PA: pre-aged spec. at 823 K for 1225 hrs

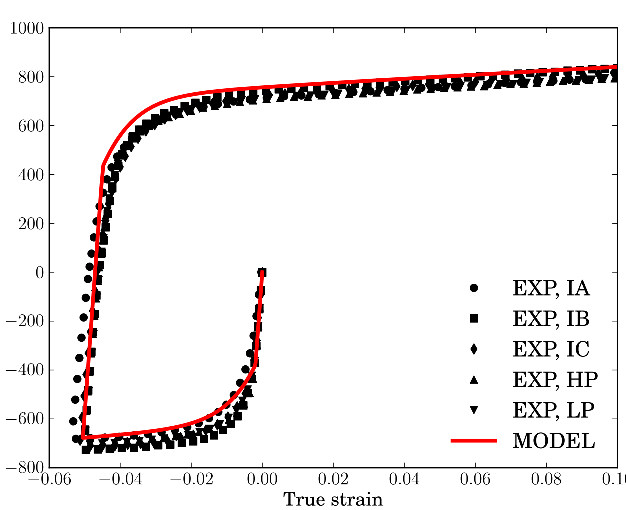

Fig. 3. Stress/strain responses at RT of the five cold-rolled materials (MODEL describes the predicted behaviour to be discussed later in the text).

$$\overset{\nabla}{\mathbf{T}} = \mathscr{L} : (\mathbf{D} - \mathbf{D}^p) \tag{1}$$

where, $\mathbf{D}$ and $\mathbf{D}^p$, are the total deformation rate and the viscoplastic deformation rate tensors, respectively, and $\mathscr{L}$ is the fourth order isotropic elasticity tensor.

The equivalent viscoplastic strain rate, $\tilde{\dot{\varepsilon}}^p$, can be written in its functional form in terms of the Kirchhoff stress tensor, $\mathbf{T}$, the absolute temperature, θ, and three microstructure-related internal variables: a mean dislocation density, ρ, the volume fraction of twins, f, and a tensorial internal stress or back stress tensor, $\mathbf{B}$. Then,

$$\tilde{\dot{\varepsilon}}^p = \hat{\tilde{\dot{\varepsilon}}}^p\{\mathbf{T}, \theta, \rho, f, \mathbf{B}\} \tag{2}$$

The above equation defines the magnitude of the inelastic flow, which combined with its direction, completes the relation for the inelastic deformation rate tensor,

$$\mathbf{D}^p = \frac{3}{2}\tilde{\dot{\varepsilon}}^p \frac{(\mathbf{T}' - \mathbf{B})}{\tilde{\sigma}^e} \tag{3}$$

where, $\mathbf{T}'$, is the deviatoric component of the Kirchhoff stress tensor and, $\tilde{\sigma}^e = \sqrt{\frac{3}{2}(\mathbf{T}' - \mathbf{B}) : (\mathbf{T}' - \mathbf{B})}$, the equivalent effective stress.

Furthermore, the equivalent viscoplastic strain rate, $\tilde{\dot{\varepsilon}}^p$, is assumed to be composed of a contribution due to the slip arising from dislocation motion in the untwinned material, $\tilde{\dot{\varepsilon}}^p_g$, and due to mechanical twinning. Here,

$$\tilde{\dot{\varepsilon}}^p = (1 - f)\tilde{\dot{\varepsilon}}^p_g + \frac{\gamma_p}{\sqrt{3}M}\dot{f} \tag{4}$$

where, γ_p, is the shear deformation induced by the slip of a partial dislocation, and, M, the Taylor factor which accounts for the polycrystalline nature of the microstructure. The viscoplastic strain rate component due to slip, $\tilde{\dot{\varepsilon}}^p_g$, accounts for the thermally activated motion of dislocations through the following expression,

$$\tilde{\dot{\varepsilon}}^p_g = \tilde{\dot{\varepsilon}}_0 \exp\left\{-\frac{G_0}{\mathcal{K}\theta}\left[1 - \left\langle\frac{\tilde{\sigma}^e - S}{\sigma_0}\right\rangle^p\right]^q\right\} \tag{5}$$

where, S, is the athermal deformation resistance that can be functionally expressed as,

$$S = \hat{S}\{\rho, f\} \tag{6}$$

$\mathcal{K}$, is the Boltzmann constant, and $\tilde{\dot{\varepsilon}}_0$, G_0, σ_0, p and q, are material parameters. Finally, the evolutionary equations of the model internal variables can similarly be written functionally as,

$$\dot{\rho} = \hat{\dot{\rho}}\left\{\tilde{\dot{\varepsilon}}^p_g, \theta, \rho, f\right\} \tag{7}$$

$$\dot{f} = \hat{\dot{f}}\left\{\tilde{\dot{\varepsilon}}^p_g, \theta, f\right\} \tag{8}$$

$$\dot{\mathbf{B}} = \hat{\dot{\mathbf{B}}}\{\mathbf{D}^p, \theta, \rho, f\} \tag{9}$$

The constitutive model was fully calibrated for the 293–873 K temperature range only for one of the five steel grades studied in this work, namely the IA grade steel (see details in Ref. [41]). Due to the fact that the uniaxial stress-strain behaviour of the five steels at room temperature was found to be similar (*e.g.* see Fig. 3), the constitutive model calibrated for the IA steel was also used to describe the behaviour of all the other four steels at room temperature. Note that a comparison of the measured and predicted temperature-dependent stress relaxation behaviour of the IA grade

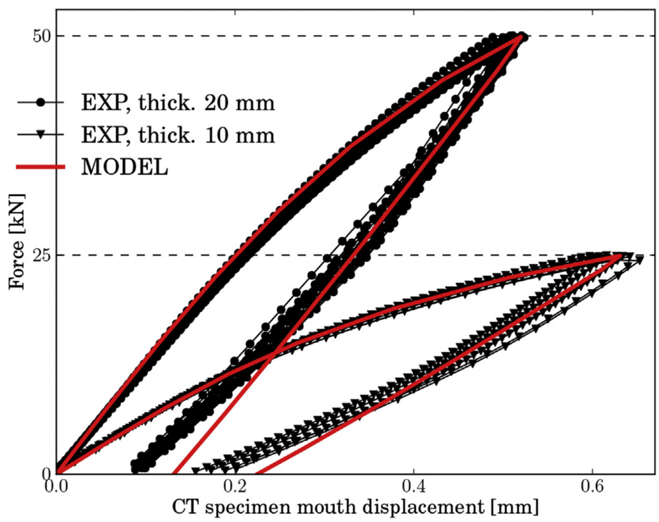

Fig. 4. Measured and predicted force/displacement responses of the CT specimens during loading at RT.

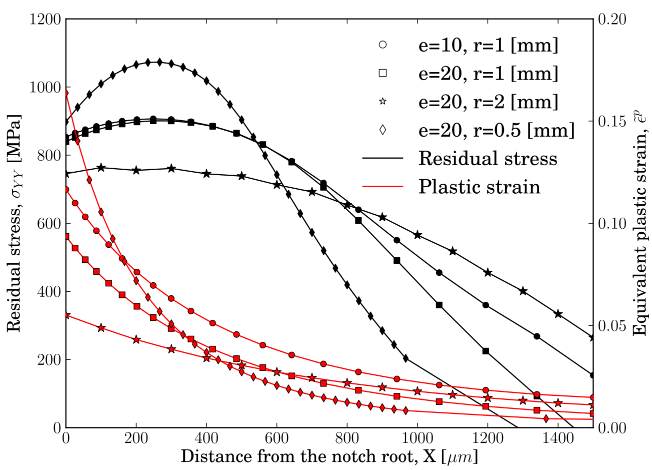

Fig. 5. Predicted residual stresses, σ_{YY}, and equivalent accumulated plastic strain, $\tilde{\varepsilon}p$, at the notch root and mid-thickness in the four different CT specimen geometries upon unloading at RT.

steel is given in Refs. [41], and that of the other four steel grades in Ref. [42].

All the measured CT specimen force/displacement responses are presented in Fig. 4. Here, the compressive force and the CT relative mouth opening displacement are given in absolute values. The resulting strain and stress fields upon unloading at the notch root region of CT specimens along the X-direction are shown in Fig. 5. The 10 and 20 mm-thick specimens with a 1 mm notch radius have similar σ_{YY} residual stress distributions up to about 800 μm from the notch root. The predicted σ_{YY} residual stresses in all CT geometries show a maximum ahead of the notch root at about 300 μm from its surface. For the 20 mm-thick specimens, it was found that the smaller the notch radius, the higher the residual stresses and the smaller the tensile region along the X-direction. Thus, for the 0.5, 1 and 2 mm notch radii, the maximum residual stresses at RT were found to be 1100, 940 and 780 MPa, respectively.

3.3. Quantitative indication of the existence of residual stresses

After the compression of the IB grade CT specimen (e = 20 mm, r = 1 mm) at RT, microhardness measurements were performed in its notch root region. Fig. 6 shows the 100 g Vicker's microhardness map obtained by extrapolating the experimentally measured values using the natural neighbour method. The tensile residual stress field presence at the CT specimen surface is revealed by a decrease in microhardness values in the notch root region. This result may seem surprising since this zone experienced a higher plastic deformation than the base material and thus should have strain hardened more. However, it was shown experimentally [43,44] and numerically [45,46] that tensile residual stresses can decrease the apparent material hardness. Some authors [1,38] measured (after thermal exposure) a hardness increase in RC-affected regions.

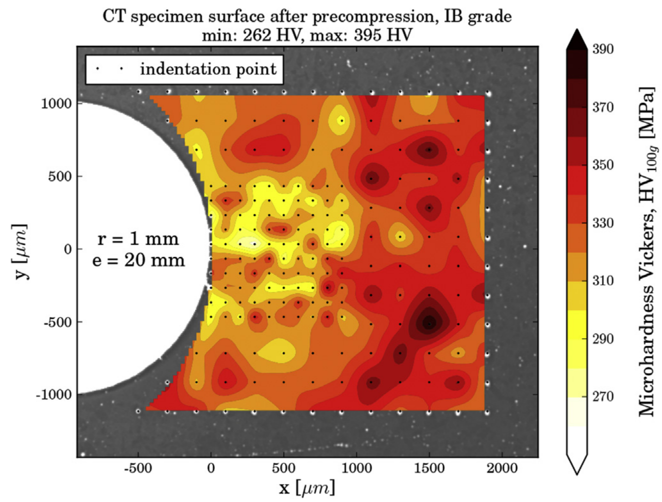

Fig. 6. Microhardness map in the notch root region of IB grade CT specimen after compression.

3.4. Stress relaxation kinetics

Stress relaxation tests were performed on IB, IC and IA grade axisymetric specimens at 823 and 873 K. These specimens had a round section of 3 mm diameter and were machined from the cold-rolled plates along the RD. The tests were conducted as follows. When the temperature attained a stable level (±0.5 K), the specimens were loaded at a strain rate of 10^{-3} s^{-1} up to 5% true strain, which corresponds approximately to the value predicted by FE in the notch root region of the CT specimens (see Fig. 5). Then, the strain was kept constant for at least 350 hrs. The experimental results are shown in Fig. 7(a). The measured stress relaxation results were used to identify the true viscoplastic strain rate of the IB, IC and IA steel grades at 823 and 873 K, as a function of the true stress (see Fig. 7(b) and (c)). In these figures, the experimental data were linearly fitted in order to identify the slopes of the $\log\sigma$ *vs* $\log\dot{\varepsilon}^p$ curves, and hence, the inverse strain rate sensitivity of the different steels. It should be noted that the prediction of the CT specimen force-displacement responses and residual stresses in the notch root regions relied on the FE calculations carried out with the internal variable-based constitutive model previously outlined and reported in Ref. [41]. For all grades, the Young's modulus used to calculate the viscoplastic strain rates was 153 GPa at 873 K and 157 GPa at 823 K [41]. In Fig. 7(b) and (c), the IA and IB grades stress relaxation rates exhibit a change in the slope of the $\log\sigma$ *vs* $\log\dot{\varepsilon}^p$ curves at approximately ~ 10^{-8} s^{-1} while that of the IC grade remains constant. At low stresses, the slopes seem to be unaffected by temperature in all cases. The results of those tests show that the stresses relax faster in the IA than in IB and IC grades, which is consistent with their higher nitrogen contents [47]. Stress relaxation tests were not performed on the HP and LP grades, but their

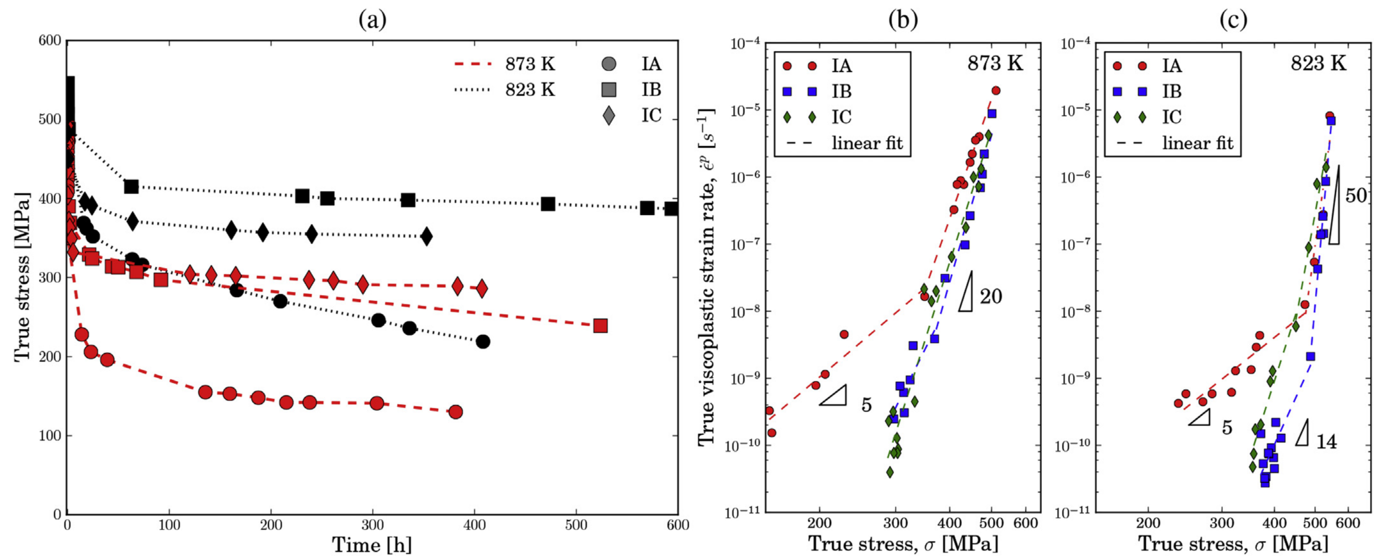

Fig. 7. Experimental stress relaxation behaviour of the IB, IA and IC grade steels at 823 and 873 K: (a) true stress *vs* time, and the corresponding (b) (c) true viscoplastic strain rate *vs* true stress at, respectively, 873 and 823 K.

high temperature behaviour is expected to be similar to those of the IC and IB grades due to their close nitrogen and carbon contents.

4. Intergranular damage

4.1. Mid-thickness damage analyses

This section presents the intergranular damage analyses performed on the mid-thickness surfaces of the tested CT specimens. The optical micrograph presented in Fig. 8(a) shows a typical mid-thickness surface of a damaged CT specimen (IB grade specimen with e = 20 mm and r = 1 mm, tested at 848 K for 3621 hrs). Damaged GBs, approximately oriented normally to the loading direction (Y) can be observed. Close-up SEM observations of microcracks show that they result from the coalescence of microcavities (see Fig. 8(b)). The intergranular nature of damage was confirmed by EBSD analyses (see Fig. 8(c)). For the same testing conditions, higher amount of RC damage was observed in the 0.5 mm-notched IB specimen (see Fig. 9). Here, the higher initial residual stresses led to the development of a macroscopic intergranular crack oriented along the X-direction (~ 750 μm long). At both sides of this intergranular macrocrack, disconnected intergranular microcavities and microcracks were observed. Those observations highlight the discontinuous nature of RC damage which begins by the nucleation of intergranular microcavities, which then coalesce into microcracks and can potentially merge to form a macrocrack.

Table 2 summarises the CT specimen testing conditions. Each specimen is represented by its steel grade name with information about its thickness and notch radius. In this work, we consider that a CT specimen is damaged if a microcavity is observed optically on the mid-thickness surface of the CT specimen. All the specimens indicated in boldface red were found to have developed

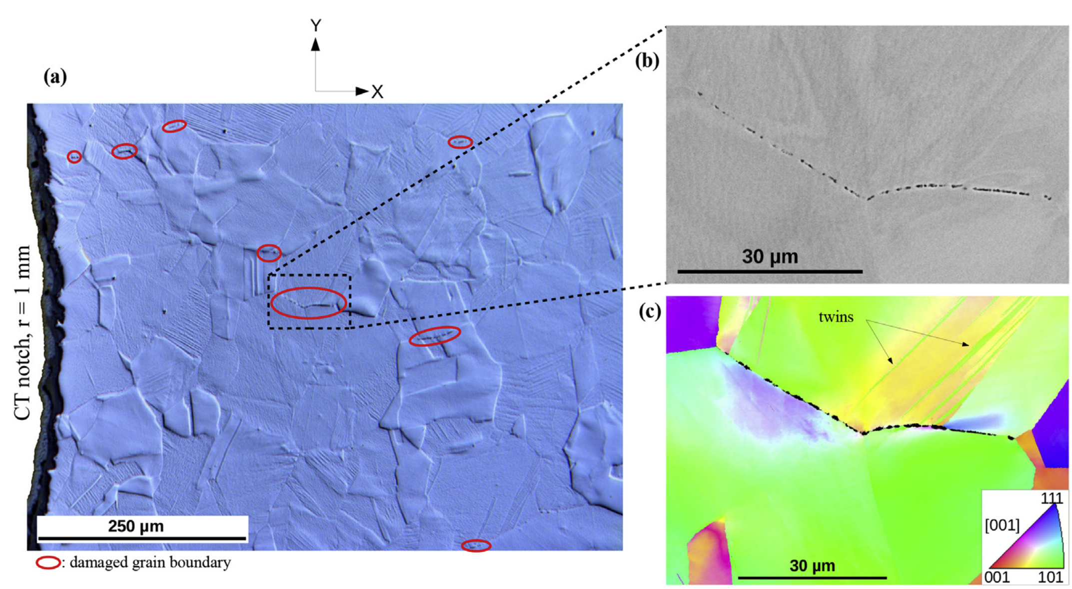

Fig. 8. (a) Mid-thickness optical micrograph of the IB grade CT specimen tested at 848 K for 3621 hrs (e = 20 mm, r = 1 mm), (b) intergranular microcavities observed by SEM and (c) IPF EBSD map of the microcavities shown in (b) (IPF colour-coded figure is shown in the inset).

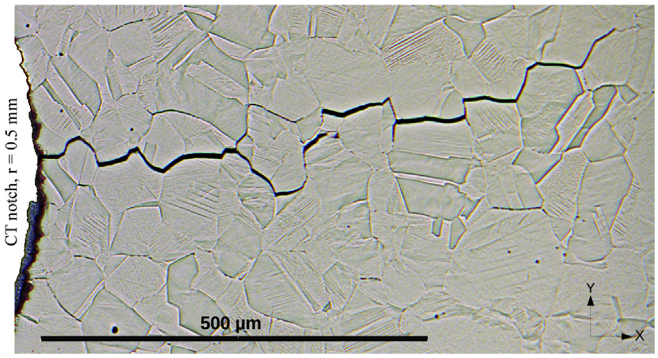

Fig. 9. Mid-thickness optical micrograph of the IB grade CT specimen tested 3621 hrs at 848 K (e = 20 mm, r = 0.5 mm) showing a macroscopic intergranular crack.

intergranular damage.

Amongst the forty-five tested CT specimens, intergranular microcavities or microcracks were observed in only sixteen of them. Intergranular damage was mostly identified in IB grade specimens and, to a lesser extent, in IA grade ones. The IC, HP and LP grade specimens did not develop any intergranular damage after five month exposure at either 823, 848 or 873 K. Since no damaged was observed in the HP and LP grade specimens, it was concluded that the level of P has no effect under tested conditions. In order to test the HP and LP grades under more detrimental conditions, two coupons cut from the HP and LP cold-rolled plates were pre-aged at 823 K for 1225 hrs before machining two new CT specimens of each. After the residual stress introduction, they were exposed at 823 and 873 K for 1455 hrs (see Table 2). In those specimens, initial GB strength was expected to be lower at the beginning of thermal exposure and thus a greater amount of intergranular damage was expected to develop subsequently. This pre-ageing actually enabled the development of RC microcavities in the HP grade specimens, while LP grade specimens remained undamaged. Finally, a ranking of RC grade resistances can then be made from the microstructural observations (from the least to the most resistant grade): IB, IA, HP and indistinctly, IC and LP.

4.2. Grain boundary analyses

Fig. 10 shows the microcavities observed by EBSD (superposition of IPF and IQ maps with a step size of 100 nm) at 150–700 µm from the notch root in the HP grade specimen pre-aged and tested at 823 K. The microcavity sizes are about 1 ± 0.5 µm and no correlation between the intersections of GBs and deformation twins with their nucleation sites is observed. Here, the deformation twins, which were not reported in RC-affected zones of industrial welded parts [38], do not seem to alter the microcavity nucleation mechanism.

SEM observations of IB and IA grade specimens revealed that microcavities and microcracks contained intergranular particles (< 200 nm in diameter) on their inner surfaces after testing at either 823, 848 or 873 K. From TEM observations, such particles were identified as $M_{23}C_6$ carbides, where, M, stands for a combination of Cr, Fe, Mo and Ni atoms (composition $(Cr_{16}\ Fe_4\ Mo_2Ni)C_6$ as determined by EDS). The crystallographic structure was identified as FCC with a lattice parameter of 10.7 Å. TEM observations through a thin section taken from within the maximum residual stress zone (from IB grade, e = 20 mm, r = 1 mm CT specimen, tested at 848 K for 3621 hrs) revealed that $M_{23}C_6$ carbides serve as nucleation sites for nanocavities (see Fig. 11). In this figure, the observed nanocavity mean diameter is approximately 50 nm.

Since poor grayscale chemical contrast exists between $M_{23}C_6$ carbides and the matrix, their observation by SEM is difficult on polished surfaces. However, the opening of microcracks by plastic

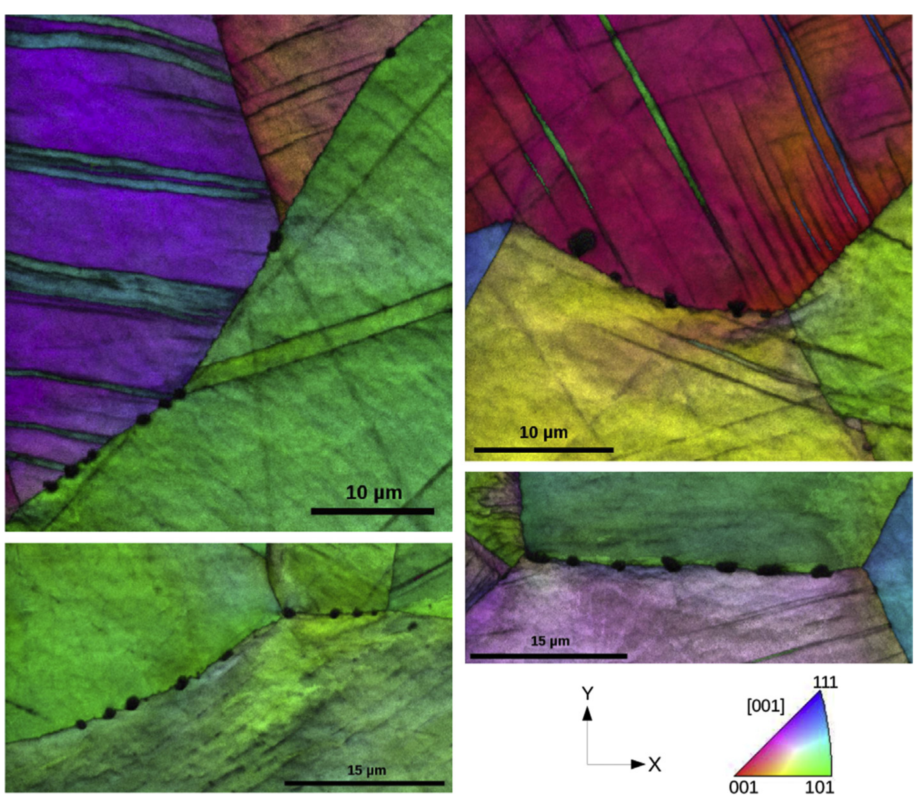

Fig. 10. Superposition of EBSD IPF and IQ maps of regions exhibiting microcavities in the HP grade specimen (e = 20 mm, r = 1 mm) pre-aged at 823 K for 1225 hrs and tested at 823 K for 1455 hrs.

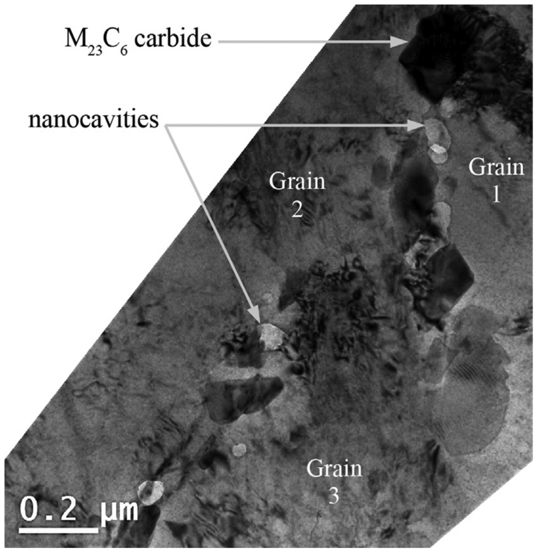

Fig. 11. Intergranular $M_{23}C_6$ carbides and nanocavities observed by TEM.

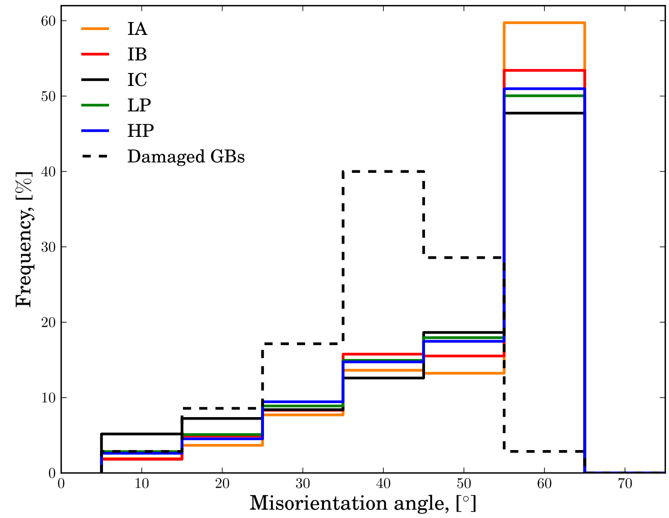

Fig. 13. Comparison between the global distributions of GB misorientations measured by EBSD in the five austenitic stainless steels (~ 61 mm of GB measured on 1 mm^2 for each grade) and those of 35 damaged GBs identified in the IB, IA and HP steels.

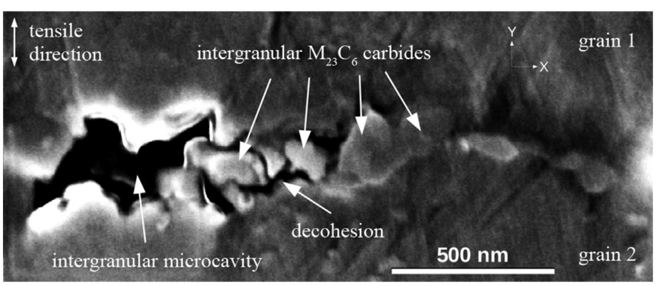

Fig. 12. SEM image showing the partial decohesion between intergranular $M_{23}C_6$ carbides and their adjacent grains on the surface of a tensile specimen deformed *in situ* up to 11% true plastic strain (IA grade specimen, e = 20 mm, r = 1 mm, tested at 823 K for 4313 hrs).

deformation in the *in situ* SEM tests enabled the $M_{23}C_6$ carbides to be observed since they protruded out of the microcrack inner surfaces. An example of a microcrack opened during the *in situ* SEM test is given in Fig. 12. This micrograph shows that RC damage results from a decohesion between coarse $M_{23}C_6$ carbides and their adjacent grains. From the experimental observations, it was concluded that the damage observed in the *in situ* SEM studies could only have evolved from grain boundary crack-like defects identified after the stress relaxation tests, e.g. see Fig. 8(a). This is supported by the fact that, after the *in situ* tomography test, no damage was seen outside the regions exposed to high levels of tensile residual stresses. In addition, all RC damage was found to consist of the same rather flat intergranular crack-like defects, and no evidence of ductile damage was found at coarse particle sites (*e.g.* MnS inclusions), which would have resulted in more spherical shaped cavities.

The GB misorientation distributions of the five AISI 316L-type austenitic stainless steels were measured and compared with the misorientation distributions of 35 damaged GBs. The results are given in Fig. 13. The GB misorientation distributions of the five steel grades are similar and ~ 50% are recrystalisation twin boundaries ($\Sigma 3$ twin, 60°/<111> in FCC material). The damaged GB misorientations reveal that the misorientations between 25 and 55° are detrimental to GB strength whereas no $\Sigma 3$ GB was found to be damaged, even though they represent about 50% of the total.

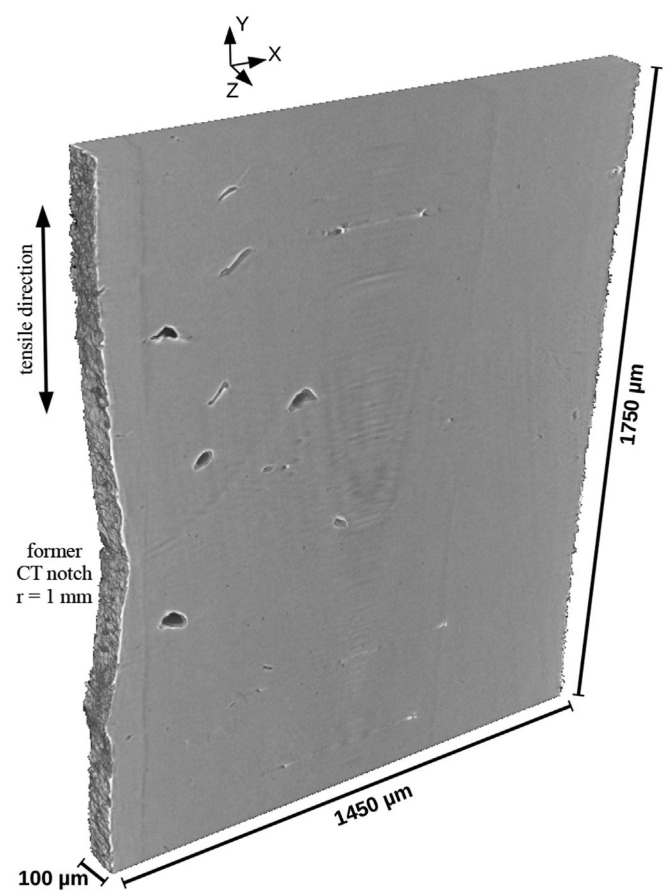

Fig. 14. 3D synchrotron tomography data rendering in the notch root region of the former IB grade CT specimen (e = 20 mm, r = 1 mm) tested at 823 K for 2946 hrs and subsequently deformed *in situ* up to 19% true plastic strain.

4.3. Damage observations by synchrotron tomography

This section presents the results of intergranular damage visualisation by X-ray synchrotron tomography in tensile specimen

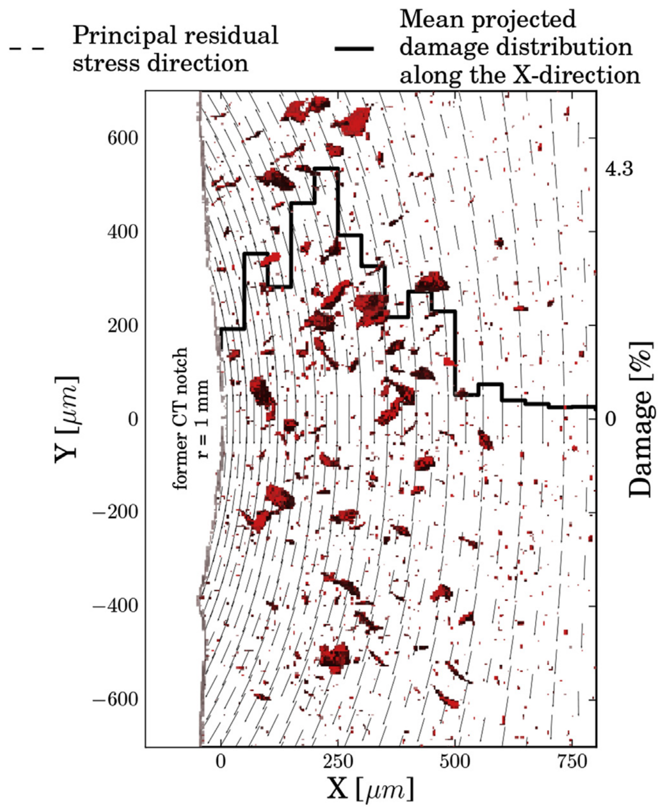

Fig. 15. Comparison between the projection of intergranular damage identified by synchrotron tomography (500 μm-thick scan) and the initial maximum principal residual stress directions (upon unloading at RT) in the notch root region of the IB grade CT specimen (e = 20 mm, r = 1 mm) tested at 848 K for 3621 hrs.

machined from the tested CT specimens and subsequently deformed *in situ*. Fig. 14 shows a 1450 × 1750 × 100 μm^3 slice of the notch root region of the IB grade CT specimen tested at 823 K for 2946 hrs and deformed *in situ* by up to 19% true strain. This technique enables the observation of microcracks in 3D using grayscale contrast. Note that damage appears darker than the bulk material.

A grayscale threshold level was used to create binary volumes where the matrix material is transparent and the damage is coloured. Fig. 15 shows the damage projection along the Z-direction, in the notch root region of the IB grade CT specimen (e = 20 mm, r = 1 mm) tested at 848 K for 3621 hrs and *in situ* deformed by up to 23% true strain along the Y-direction. Here, the thickness of the projected slice is 500 μm. The additional homogeneous distribution of small particles that also appear coloured were identified as MnS inclusions. In this image, the black-dashed curves represent the maximum principal residual stress directions before thermal exposure predicted by the FE analysis. Good agreement is observed between the microcracks normal directions and the maximum principal residual stress directions. These results show that GB sliding is unlikely to be important under RC conditions. Furthermore, the black curve shows the distribution of intergranular damage along the X-direction. In order to quantify the intergranular damage, the scanned volume was first divided into 50 μm cubes (15 along the X-direction, 24 along the Y-direction and 10 along the Z-direction). In each cube, the microcracks were projected along the Y-direction on the bottom face (XZ). The damage was defined by the ratio of the projected-microcrack surface to the cube face area (50 × 50 μm^2). Finally, the damage distribution along the X-direction was obtained by averaging the damage values through the thickness (Z) and then averaging them along the Y-direction. The resulting maximum damage region is in good agreement with the predicted maximum initial residual stress distribution (see Fig. 5).

The influence of the testing temperatures and initial residual stress magnitudes in the IB grade CT specimens were studied by synchrotron tomography. The results are given in Fig. 16, which shows a comparison between the damage projections and the predicted principal residual stresses obtained by FE. Here, Fig. 16(a), (b) and (c) correspond to 20 mm-thick CT specimens with notch radii of 1 mm and tested at 873, 848 and 823 K, respectively, for 3621 hrs. The specimen tested at the intermediate temperature of 848 K (Fig. 16(b)) exhibits a higher degree of damage than the others. This result was also confirmed when observing by SEM the three IB grade CT specimens tested at the same temperatures for 1455 hrs. Here the most detrimental temperature for RC resistance seems to be around 848 K for the IB grade steel. The Fig. 16(e) and (f) maps correspond to 20 mm-thick CT specimens tested at 848 K for 3621 hrs, with notch root radii of 2 and 0.5 mm, respectively. The higher value of the principal residual stress in the 0.5 mm-notched specimen resulted in a higher amount of intergranular damage (same specimen as in Fig. 9), whereas the 2 mm-notched specimen exhibits less damage than the 0.5 and 1 mm-notched specimens (Fig. 16(f) and (b), respectively). In all maps, the initial threshold level of principal residual stress that led to RC damage development was estimated from the different threshold values identified by the black-dashed lines in Fig. 16 at 740 ± 30 MPa.

5. Discussion

5.1. Effect of cold rolling

The initiation of RC damage is known to occur in high residual stress regions at or near GBs which have been plastically deformed (*e.g.* Ref. [38]). However, to achieve the initial residual stress level needed to develop RC (about four times the material yield strength at room temperature for the less RC-resistant grade steels tested in this work), it is generally required that the material be strain hardened prior to service. Evidence to that effect is the high hardness levels measured in actual RC affected regions [1,38] and the TEM observations of increased dislocation densities in the HAZ of an AISI 316L(N) weld reported by Ref. [38]. It should also be noted that all the materials in this study were pre-conditioned by cold rolling whereas RC affected regions in the HAZ of actual components undergo thermal loadings (*e.g.* during multipass welding) that may involve several cycles leading to plastic deformations at moderate-to-high temperatures. SEM observations of the cold-rolled material were carried out and revealed that no GB damage (*i.e.* microcavities) was present using the peak resolution of the SEM. In addition, no damage was observed after the residual stress relaxation tests in the IC and LP steels that posses similar mechanical properties as the other tested steels where RC damage was found. Thus, it can be concluded that GB damage could not have been introduced either as a result of the plastic deformation of the CT specimen during the room temperature compression test. Even though SEM-EBSD observations revealed that the material cold rolling introduced mechanical twins in the microstructure, their presence was not found to have affected the main intergranular damage mechanisms responsible for RC in the austenitic stainless steels (*e.g.* GB microcavity nucleation at intergranular carbides). These observations support the understanding that the use of cold rolled materials is suitable to study RC, at least from a mechanical point of view since the chemical characteristics of actual HAZ GBs may be affected by the thermal cycling of the HAZ regions during welding. Concerning the latter, it is also worth noting that a typical welding cycle in a 316L(N) steel has been reported to last typically

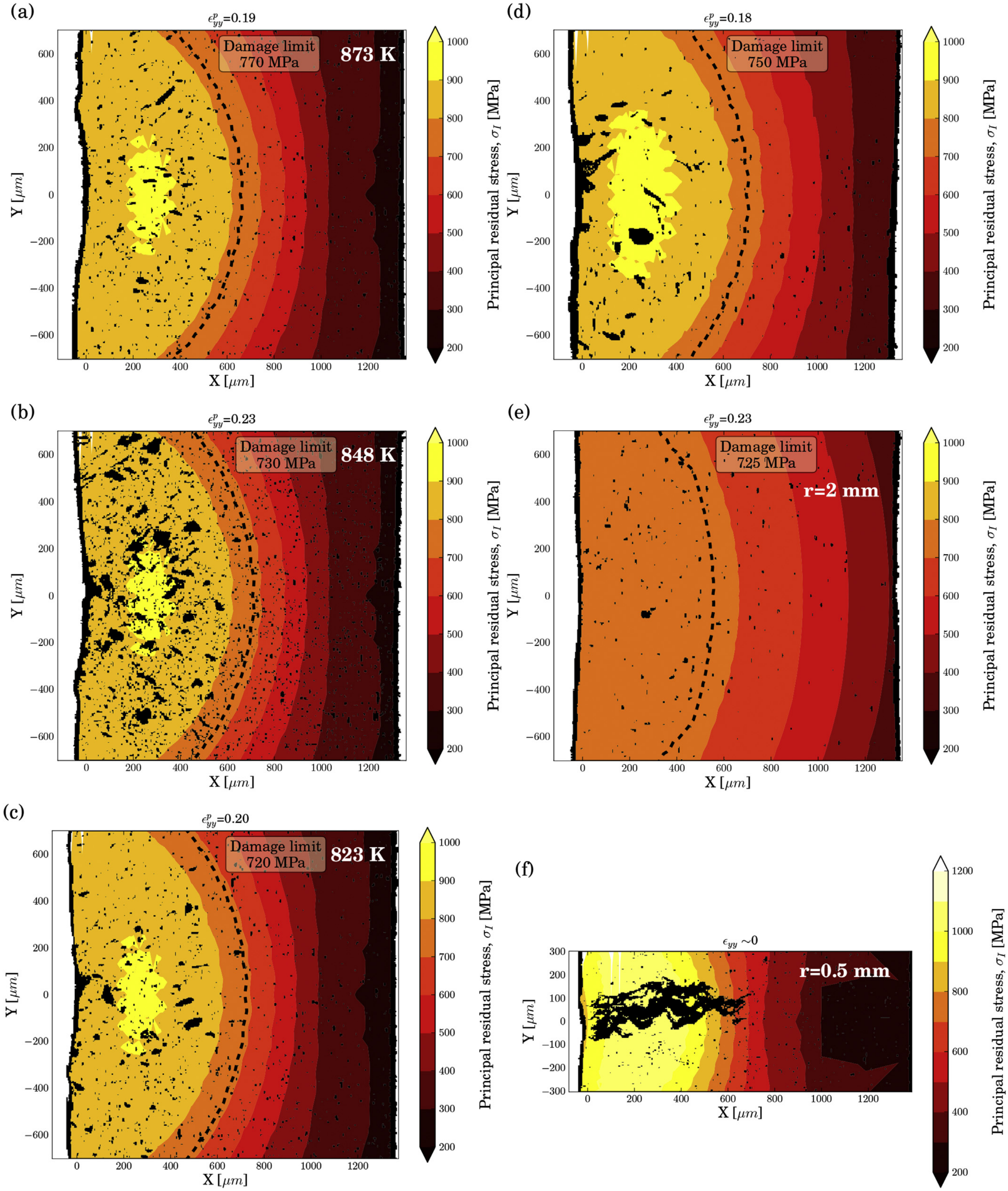

Fig. 16. Comparison between the projection of intergranular damage obtained by synchrotron tomography (500 μm-thick scans) and the initial principal residual stresses (upon unloading at RT) in the notch root region of IB grade CT specimens with (a) (b) (c) e = 20 and r = 1 mm, tested at 873, 848 and 823 K, respectively, for 3621 hrs and with (d) e = 10 and r = 1 mm, tested at 848 K for 1455 hrs and with (e) (f) e = 20 mm and notch radii of 2 and 0.5 mm, respectively, tested at 848 K for 3621 hrs.

only a couple of seconds and the peak HAZ region temperature to be approximatively 923 K [38].

5.2. Chemical composition and temperature effects

The results of the RC experiment performed on the CT-like

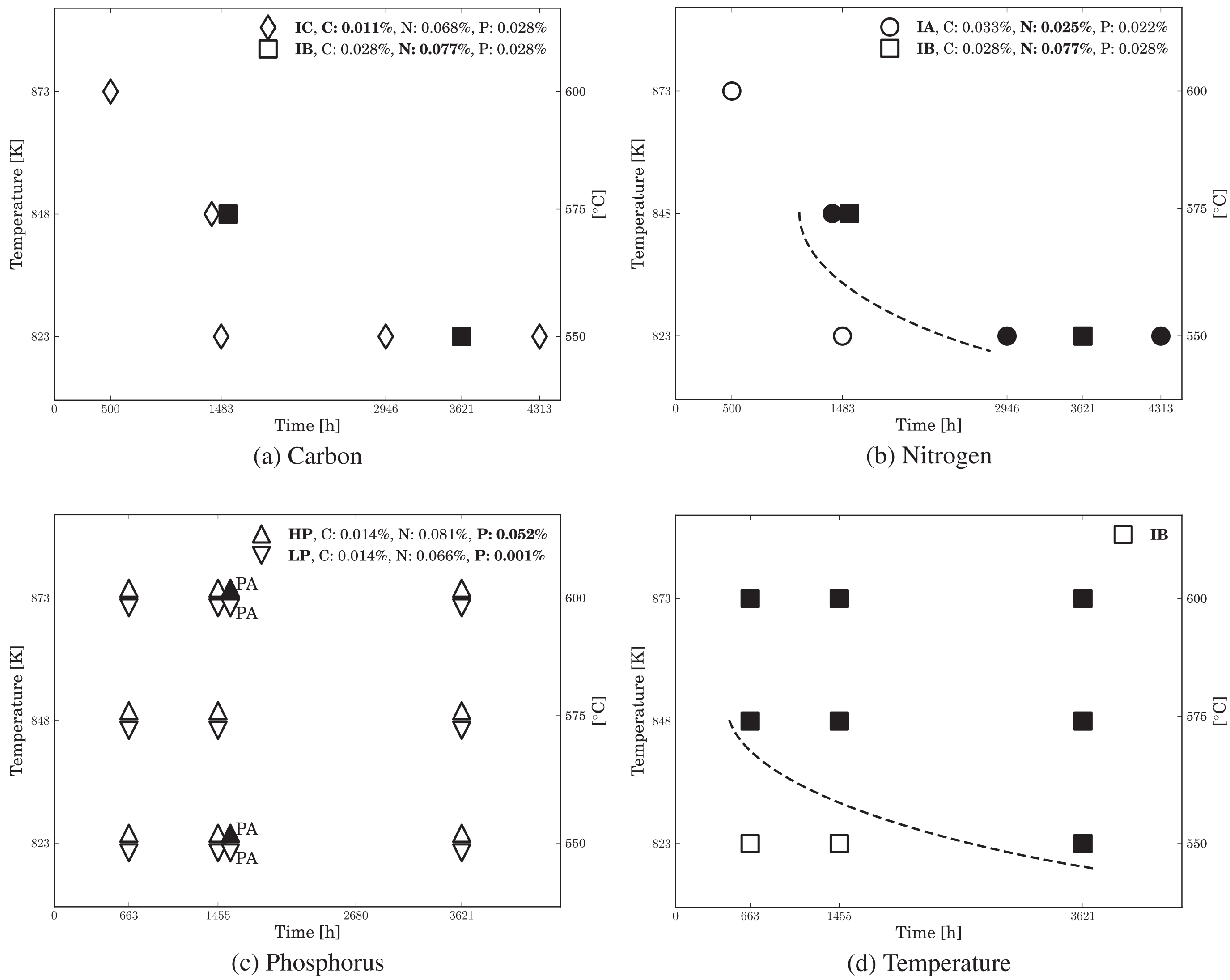

Fig. 17. Effect of (a) carbon, (b) nitrogen, (c) phosphorus and (d) temperature on RC damage development. Open symbols indicate undamaged specimens and filled ones damaged. PA: pre-aged spec. at 823 K for 1225 hrs.

specimens showed evidence of GB degradation by intergranular carbide precipitation and, to a lesser extent, P segregation, when tested in the 823–873 K temperature range. Furthermore, the stress relaxation rates were found to decrease with high N contents, thus the lowest relaxation rates being in the high N grade steels (IB and IC). Reheat cracking damage development is next discussed based on the results summarised in Fig. 17. Here, the data from Table 2 are presented so as to compare the respective effect of C, N and P contents on RC damage development. Fig. 17(a), (b) and (c) shows the results of damage observation in specimens whose chemical composition differ only in the C, N and P contents, respectively. In each subfigure, the CT specimen geometry is identical. In Fig. 17(d), the effect of temperature on RC damage development is based on the results obtained in the IB grade specimens.

5.2.1. Carbon effect

Fig. 17(a) shows the effect of C content in RC damage development (for e = 10 mm and r = 1 mm CT specimens). In the same conditions, the IB grade which has a high C content (0.028%) exhibits intergranular damage while the IC one (0.011% C) does not. The N and P content being similar, the lower resistance of IB grade is attributed to its higher intergranular carbide precipitation which decreases GB strength. At the microstructural scale, this observation is confirmed by the higher propensity to RC of the 25 to 55° misoriented GBs (see Fig. 13), which are preferential surfaces for $M_{23}C_6$ carbide precipitation. Likewise, the lower propensity of Σ3 GBs to RC is consistent with the fact that they are hardly affected by $M_{23}C_6$ carbide precipitation. The detrimental effect of high C content has also been confirmed by TEM observations since they revealed that $M_{23}C_6$ carbides are preferential sites for nanocavity nucleation (see Fig. 11).

5.2.2. Phosphorus effect

Without pre-ageing, HP and LP grades did not develop intergranular damage (see Fig. 17(c)). However, higher P content was found to increase microcavity nucleation as observed in the pre-aged HP grade steel. The P segregation levels expected at GBs in the HP grade steel was predicted using the Langmuir-McLean model (see Appendix A). The diagram shown in Fig. 18 represents the predicted P monolayer coverage as a function of temperature and ageing time. For HP steel grade, P monolayer coverage in the tested CT specimens was expected to be about 37–41% after ~

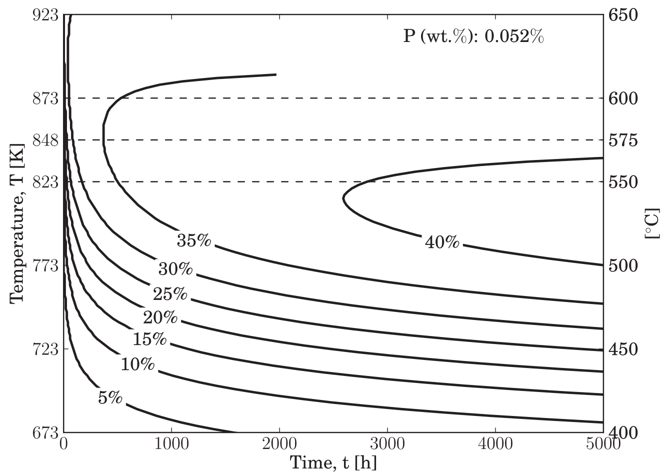

Fig. 18. Isolines of constant P monolayer coverage in a time/temperature diagram predicted by the Langmuir-McLean model in an austenitic stainless steel with a P bulk content of 0.052%.

3600 hrs at 823–873 K. However, in low alloy steels, a threshold value in P monolayer coverage (~ 5–10%) below which no intergranular damage is observed was found [48,49]. Therefore, if we consider this threshold value as that which would trigger intergranular damage development under RC conditions, the P monolayer coverage prediction of the HP grade should be inaccurate.

The P monolayer coverage model takes no account of the individual effects of other solute elements present in AISI 316L-type steel: in austenite, some authors reported P–C repulsion interaction at GBs [50–53] or site-competing segregation mechanisms, such as P–B [51,54] or P–N [27,55–57]. Latter work by Briant et al. [57] showed that phosphorus segregation can clearly be inhibited by the additions of N in 304L and 316L-type austenitic stainless steels. In order to determine the predominant segregation interaction in our 316L-type IB and HP steels, measurements of the P, N and B monolayer coverage by Auger electron spectroscopy were attempted but gave no conclusive results due to the tendency of austenitic stainless steel to undergo ductile fracture at low temperatures. An understanding of the site-competing segregation mechanisms involving P, C, N and B will be addressed in future work.

5.2.3. Nitrogen effect

Fig. 17(b) shows the N content effect on RC damage development (for e = 10 mm and r = 1 mm CT specimens). In the same conditions, the IB grade which has a high N content (0.077%) presents more intergranular damage than the IA (0.025% N). Even though CT specimens of both grades developed damage under the same testing conditions, microstructural observation by SEM and synchrotron tomography shows that the IB grade exhibits much more intergranular damage than the IA. The C contents being similar, the GBs should contain an equivalent number of sites ($M_{23}C_6$ carbides) for nanocavity nucleation. However, the lower stress relaxation rate (see Fig. 7) induced by the high N content in the IB steel grade should enable high residual stresses at GBs to be maintained for a longer time and thus increase the number of nanocavities. According to the discussion results of Section 5.2.2, high N content could therefore have two contrasting effects on RC resistance: a detrimental one due to low stress relaxation rate and a beneficial one as it could impede intergranular P segregation by a site-competing mechanism.

5.2.4. Temperature effect

Fig. 17(d) shows the effect of temperature in RC damage development (for e = 20 mm and r = 1 mm IB grade CT specimens). At 823 K, no intergranular damage was observed before ~ 3600 hrs but after ~ 660 h at 848 and 873 K. In addition, higher amount of damage was observed in the IB grade CT specimen tested at the intermediate temperature of 848 K than those tested at either 823 or 873 K for ~ 660 to ~ 3600 hrs. To explain this detrimental effect of the intermediate testing temperature on RC, it should be noted that the intergranular damage mechanisms identified here ($M_{23}C_6$ carbide precipitation, stress relaxation controlled by the amount of N in solid solution and, to a lesser extent, P segregation) are diffusion-controlled. Fig. 19 shows a proposed schematics to explain the existence of the most detrimental temperature to minimise the time of the RC damage onset. At temperature T_i (for i = 1,2 or 3), the RC damage is assumed to start at time, t_i, when the residual stress curve, $\sigma(t,T_i)$, intersects the GB strength one, $S_{GB}(t,T_i)$. The temperature-dependant kinetics of those phenomea can lead to the formation of the bell-shaped curve shown as a dashed line in Fig. 19. Here, the intermediate testing temperature T_2 would enable an earliest development of RC damage than a higher temperature such as T_1. The existence of a most detrimental temperature could therefore be explained and should change with chemical composition (especially C and N) of the 316L-type austenitic stainless steels.

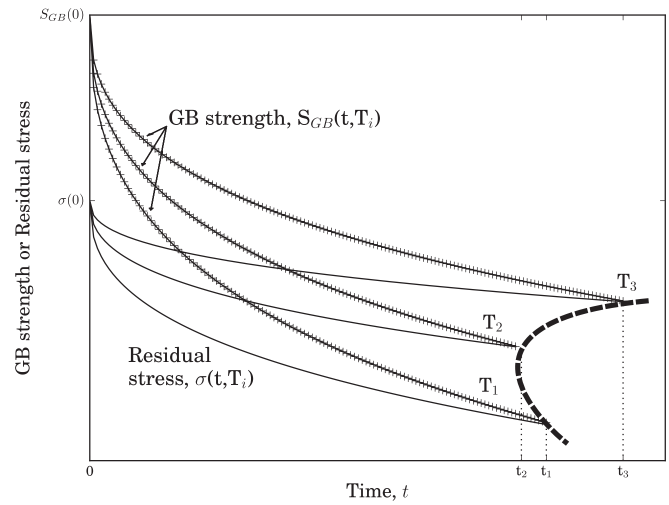

Fig. 19. Schematic of the proposed competing mechanisms arising from residual stress relaxation and GB degradation over time. The dashed line represents the *loci* of points for the onset of RC damage at different temperatures ($T_1 > T_2 > T_3$).

5.3. Susceptibility to RC of the five steel grades

The microstructural observations presented previously enable the five tested 316L-type grades to be ranked in terms of the increasing resistance to RC: IB, IA, HP and, indistinctly, LP and IC. Table 3 shows this grade ranking associated with their C, N and P contents. IC grade is the most resistant to RC in the tested conditions while IB grade been the least resistant. Those results are not surprising since the IC grade was also found to be highly resistant to creep-fatigue at 873 K while the IB grade did not [58]. In accordance with the previous discussions, Table 3 shows that high P content

Table 3
Reheat cracking resistance ranking of the five AISI 316L-type steels and their C, N and P contents (wt.%) (1 being the most resistant).

Ranking	5^{th}	4^{th}	3^{rd}	1^{st} or 2^{nd}	1^{st} or 2^{nd}
Name	IB	IA	HP	LP	IC
C	0.028	0.033	0.014	0.014	0.011
N	0.077	0.025	0.081	0.066	0.068
P	0.028	0.022	0.052	0.001	0.021

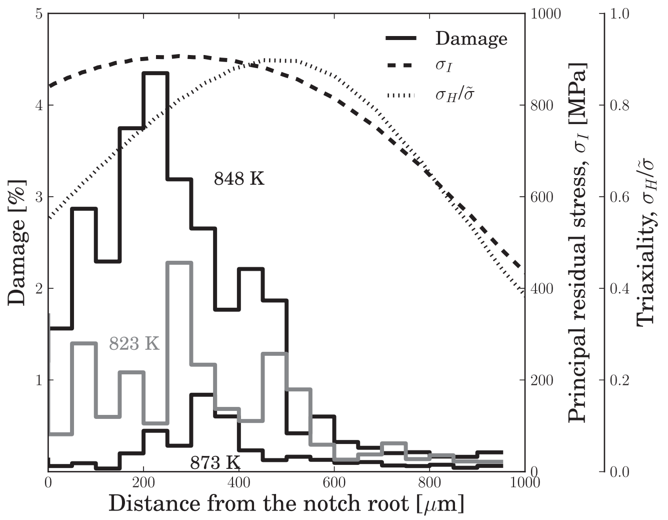

Fig. 20. Comparison between the predicted initial principal residual stress and triaxiality distributions (upon unloading at RT) and the tomography-measured damage along the X-direction from the notch root of the tested IB steel CT specimens at 823, 848 and 873 K.

has little effect on RC. The major chemical composition effects on RC susceptibility were found to be due to the C and N contents: high C content (about > 0.025%) is detrimental to GB resistance and high N content (about > 0.06%) should be added only if the C content is low (about < 0.015%).

5.4. *Effect of stress state*

Many authors have found that stress triaxiality decreases the material ductility in 316, 316H, 316L and 316L(N) steels under creep conditions [10,14–16]. In creep damage models, extended visco-plastic cavity growth is generally associated with high triaxiality levels (e.g. Ref. [59]). In contrast, in this work it was found that the maximum principal residual stress component is probably the main driving force for the development of intergranular damage under stress relaxation conditions. This can be seen from the information presented in Fig. 20, which shows a comparison between the damage measured by tomography in the IB steel specimens with a notch root of 1 mm at 823, 848 and 873 K, and the predicted distributions of the initial maximum principal residual stress, σ_I, and the stress triaxiality. Here, the latter was defined as the ratio between the mean hydrostatic stress and the equivalent Mises stress, $\sigma_H/\tilde{\sigma}$. The damage definition was that used in Fig. 15. It can be seen that the loci of maximum measured damage for the three tested temperatures are in better accordance with the location of the peak maximum principal residual stress than that of the stress triaxiality. The effect of stress state on the damage development in the tested CT specimens are studied and discussed in more detail in a separate publication [41].

6. Conclusions

The study of reheat cracking in five chemically different AISI 316L-type austenitic stainless steels was successfully performed using a compressed CT specimen technique. A comparison of the grade susceptibilities to intergranular damage development in the 823–873 K temperature range in the presence of high tensile residual stresses enabled an identification of the reheat cracking damage mechanisms to be made. They are: (i) the development of nanocavities on intergranular $M_{23}C_6$ carbides which precipitate preferentially on 25 to 55° misoriented GBs, (ii) the low stress relaxation rate which enables high residual normal stresses on GB to be maintained, and to a lesser extent, (iii) the P segregation at GBs which increases intergranular microcavity nucleation.

The use of cold rolled 316L-type steels made it possible to attain the level of residual stresses needed to develop RC in these materials without altering the above mentioned RC damage mechanisms. Furthermore, *in situ* synchrotron X-ray tomography was successfully relied upon to identify and quantify the level of intergranular damage in the specimens but only after the specimens were plastically deformed uniaxially in tension at room temperature to open up and thus render visible the intergranular microcracks.

The most detrimental operating temperature for reheat cracking damage development was found to depend on the stress relaxation behaviour and GB degradation which are directly linked to the chemical composition of the austenitic stainless steel. In particular, the intermediate testing temperature of 848 K for the AISI 316L-type IB steel was identified as the most damaging amongst the three tested temperatures under reheat cracking conditions. Furthermore, in this steel grade, a principal residual stress threshold of 740 ± 30 MPa (at RT) was identified below which no intergranular damage was found after ~ 3600 hrs in the 823–873 K temperature range. Furthermore, the effect of high P content was not found to be as detrimental as expected and could be explained by the site-competing segregation mechanisms between P, N, C and/or B. In the presence of high principal residual stresses (>740 ± 30 MPa), high C content (about > 0.025%) was found to be detrimental to GB resistance, thus high N content (about > 0.06%) should be added only if the C content of the steel is low (about < 0.015%). This work has provided information about the level of residual stresses that can lead to the development of RC in AISI 316L-type steels, and of the C, N and P contents that can be relied upon as qualitative measures for future RC models/criteria to optimise welding process models and their predictions.

Acknowledgements

This work has been financially supported by the AREVA Chair at the École des Mines de Paris. The authors would like to acknowledge Sophie Dubiez-Le Goff for her support and contributions to this work, EDF for the supply of the IB grade steel plate, the ESRF for providing beam time, as well as ESRF's researchers Lukas Helfen, Marco Di Michiel and Mario Scheel for their support in the experiments MA1932 and ME1366 performed at ID15. The help provided by the INSA-Lyon for the use of their *in situ* tensile test device is greatly appreciated. The authors would also like to thank Mohamed Sennour from the Ecole des Mines de Paris's Centre des Matériaux for his help with the TEM observations.

Appendix A. Langmuir-McLean model

The GB equilibrium monolayer coverage of the solute of interest, C_{∞}^{GB} is a function of its bulk concentration, C^B, the temperature, T, and its Gibbs energy of segregation, ΔG^0 [60]. When assuming that C^B is small, then

$$C_{eq}^{GB} = \frac{C^B exp(\Delta G^0/RT)}{1 + C^B exp(\Delta G^0/RT)}. \tag{A.1}$$

The GB monolayer coverage of the solute of interest at time t, $C^{GB}(t)$, is expressed as [60]:

Table A.4Langmuir-McLean model parameters for P segregation in γ-iron.

Parameter	Value	Reference
$\Delta G^0 = \Delta H - T\Delta S$	$\Delta H = -32$ KJ mol^{-1} $\Delta S = 17$ kJ K^{-1} mol^{-1}	[62]
$D = Aexp\left(-\frac{Q}{RT}\right)$	$A = 0.51$ cm^2 s^{-1} $Q = 230.2$ kJ K^{-1} mol^{-1}	[61]
δ	0.8 nm	[60]

$$C^{GB}(t) = C^{GB}_{eq1} - C^{B}(\alpha_1 - \alpha_0)exp\left(\frac{4Dt}{\alpha_1^2\delta^2}\right)erfc\left(\frac{2\sqrt{Dt}}{\alpha_1\delta}\right), \tag{A.2}$$

with, C^{GB}_{eqi}, the GB equilibrium concentration at temperature T_i, D, the solute diffusion coefficient in the bulk material at temperature T_1, δ, the GB thickness, $\alpha_1 = C^{GB}_{eq1}/C^B$ and $\alpha_0 = C^{GB}_{eq0}/C^B$.

The parameters used to predicted GB monolayer coverage of P were taken from the literature (see Table A.4). The diffusion coefficient, D, was identified by Heyward and Goldstein [61] in a Fe–Ni–P grade in the 1173–1473 K temperature range (austenitic phase). The Gibbs energy for the P segregation was taken from the work of Erhart and Paju [62] in Fe–P+(C,Cr, Ni,Mn,V) grades (austenitic phase).

References

[1] P. Bouchard, P. Withers, S. McDonald, R. Heenan, Quantification of creep cavitation damage around a crack in a stainless steel pressure vessel, Acta Mater. 52 (2004) 23–34.
[2] R. Curran, A. Rankin, Austenitic steels in high temperature steam piping, Trans. ASME 79 (1957) 1398–1409.
[3] R. Emerson, R. Jackson, The plastic ductility of austenitic piping containing welded joints at 1200 F, Res. Suppl. Weld. J. (1957) 89–104.
[4] R. Younger, R. Baker, Heat affected zone cracking in welded high-temperature austenitic steels, J. Iron Steel Inst. 196 (1960) 1S8.
[5] R. Younger, R. Baker, D. Haddrill, Post-weld heat treatement of high-temperature austenitic steels, J. Iron Steel Inst. 201 (1963) 693.
[6] C. Meitzner, Stress Relief Cracking in Steel Weldments, Welding Research Council Bulletin, 1975.
[7] J. Van Wortel, Relaxation Cracking in the Process Industry, an Underestimated Problem, Maintenance for Managing Life and Performance, 1998, pp. 637–647.
[8] M. Cabrillat, P. Allegre, E. Pluyette, B. Michel, Intergranular reheat cracking in 304H components. experiments and damage evaluation, Struct. Mech. React. Technol. 16 (2001).
[9] M. Coleman, D. Miller, R. Stevens, Reheat cracking and strategies to assure integrity of type 316 welded components, in: Integrity of High-temperature Welds, International Conference, Nottingham, 1998, pp. 169–179.
[10] Q. Auzoux, L. Allais, C. Caës, B. Girard, I. Tournié, A. Gourgues, A. Pineau, Intergranular damage in AISI 316L(N) austenitic stainless steel at 600°C: pre-strain and multiaxial effects, Nucl. Eng. Des. 235 (2005) 2227–2245.
[11] Q. Auzoux, L. Allais, C. Caës, I. Monnet, A. Gourgues, A. Pineau, Effect of pre-strain on creep of three AISI 316 austenitic stainless steels in relation to reheat cracking of weld-affected zones, J. Nucl. Mater. 400 (2010) 127–137.
[12] M. Chabaud-Reytier, L. Allais, C. Caës, P. Dubuisson, A. Pineau, Mechanisms of stress relief cracking in titanium stabilised austenitic stainless steel, J. Nucl. Mater. 323 (2003) 123–137.
[13] M.W. Spindler, The multiaxial creep ductility of austenitic stainless steels, Fatigue Fract. Eng. Mater. Struct. 27 (2004) 273–281.
[14] R. Moen, G. Smith, A consideration on limits of cold working in nuclear construction, J. Eng. Mater. Technol. 97 (1975) 162–171.
[15] M. Willis, A. McDonaugh-Smith, R. Hales, Prestrain effects on creep ductility of a 316 stainless steel light forging, Int. J. Press. Vessels Pip. 76 (1999) 355–359.
[16] B. Wilshire, M. Willis, Mechanisms of strain accumulation and damage development during creep of prestrained 316 stainless steels, Metall. Mater. Trans. A Phys. Metall. Mater. Sci. 35 A (2004) 563–571.
[17] R. Skelton, I. Goodall, G. Webster, M. Spindler, Factors affecting reheat cracking in the HAZ of austenitic steel weldments, Int. J. Press. Vessels Pip. 80 (2003) 441–451.
[18] R. Thomas Jr., HAZ cracking in thick sections of austenitic stainless steels–I, Weld. J. 63 (1984) 24–32.
[19] A. Dhooge, A. Vinckier, Reheat cracking – A review of recent studies, Int. J. Press. Vessels Pip. 27 (1987) 239–269.
[20] A. Dhooge, Survey on reheat cracking in austenitic stainless steels and Ni base alloys, Weld. World 41 (1998) 206–219 (Eng).
[21] B. Weiss, R. Stickler, Phase instabilities during high temperature exposure of 316 austenitic stainless steel, Metall. Trans. 3 (1972) 851–866.
[22] H. Hong, B. Rho, S. Nam, Correlation of the M23 C6 precipitation morphology with grain boundary characteristics in austenitic stainless steel, Mater. Sci. Eng. A 318 (2001) 285–292.
[23] R. Jones, V. Randle, G. Owen, Carbide precipitation and grain boundary plane selection in overaged type 316 austenitic stainless steel, Mater. Sci. Eng. A 496 (2008) 256–261.
[24] H. Hong, S. Nam, Improvement of creep-fatigue life by the modification of carbide characteristics through grain boundary serration in an AISI 304 stainless steel, J. Mater. Sci. 38 (2003) 1535–1542.
[25] K. Kim, H. Hong, K. Min, S. Nam, Correlation between the carbide morphology and cavity nucleation in an austenitic stainless steels under creep-fatigue, Mater. Sci. Eng. A 387 – 389 (2004) 531–535, 13th International Conference on the Strength of Materials.
[26] J. Hong, S. Nam, S. Choi, The influences of sulphur and phosphorus additions on the creep cavitation characteristics in type 304 stainless steels, J. Mater. Sci. 21 (1986) 3966–3976.
[27] C. Briant, Grain boundary segregation of phosphorus and sulfur in types 304L and 316L stainless steel and its effect on intergranular corrosion in the huey test, Metall. Trans. A 18 (1987) 691–699.
[28] T. Ogura, T. Watanabe, S. Karashima, T. Masumoto, Dependence of phosphorus segregation on grain boundary crystallography in an Fe–Ni–Cr alloy, Acta Metall. 35 (1987) 1807–1814.
[29] M. Herbig, M. Kuzmina, C. Haase, R. Marceau, I. Gutierrez-Urrutia, D. Haley, D. Molodov, P. Choi, D. Raabe, Grain boundary segregation in Fe-Mn-C twinning-induced plasticity steels studied by correlative electron backscatter diffraction and atom probe tomography, Acta Mater. 83 (2015) 37–47.
[30] G.R. Kegg, J.M. Silcock, D.R.F. West, The effect of phosphorus additions and cooling rate on the precipitation of $M_{23}C_6$ in austenite, Metal Sci. 8 (1974) 337–343.
[31] B. Chen, P. Flewitt, D. Smith, Microstructural sensitivity of 316H austenitic stainless steel: residual stress relaxation and grain boundary fracture, Mater. Sci. Eng. A 527 (2010) 7387–7399.
[32] J. Borland, Generalized theory of super-solidus cracking in welds (and castings), Br. Weld. J. 7 (1960) 508–512.
[33] A.H. Sherry, M. Turski, M.A. Wilkes, D.W. Beardsmore, P.J. Withers, P.J. Bouchard, The development of a compact specimen to study the influence of residual stresses on fracture, in: Engineering Structural Integrity Assessment, 2002.
[34] M. Spindler, The use of borland specimens to reproduce reheat cracking in type 316H, in: Int. Conf. On High Temperature Plant Integrity and Life Extension, 2004.
[35] S. Hossain, C.E. Truman, D.J. Smith, R.L. Peng, U. Stuhr, A study of the generation and creep relaxation of triaxial residual stresses in stainless steel, Int. J. Solids Struct. 44 (2007) 3004–3020.
[36] S. Hossain, C.E. Truman, D.J. Smith, Generation of residual stress and plastic strain in a fracture mechanics specimen to study the formation of creep damage in type 316 stainless steel, Fatigue Fract. Eng. Mater. Struct. 34 (2010) 654666.
[37] M. Turski, P. Bouchard, A. Steuwer, P. Withers, Residual stress driven creep cracking in AISI type 316 stainless steel, Acta Mater. 56 (2008) 3598–3612.
[38] Q. Auzoux, Fissuration en relaxation des aciers inoxydables austnitiques – influence de l'écrouissage sur l'endommagement intergranulaire (Ph.D. thesis), Ecole Nationale Supérieure des Mines de Paris, 2004.
[39] C. Landron, E. Maire, O. Bouaziz, J. Adrien, L. Lecarme, A. Bareggi, Validation of void growth models using X-ray microtomography characterization of damage in dual phase steels, Acta Mater. 59 (2011) 7564–7573.
[40] Zset, http://www.zset-software.com, Online (2015).
[41] H. Pommier, E. P. Busso, and T. Morgeneyer, In Preparation (2015).
[42] H. Pommier, Stress Relaxation Cracking in 316L-type Austenitic Stainless Steels (Ph.D. thesis), École nationale supérieure des Mines de Paris, 2015.
[43] T.R. Simes, S.G. Mellor, D.A. Hills, A note on the influence of residual stress on measured hardness, J. Strain Analysis Eng. Des. 19 (1984) 135–137.
[44] T.Y. Tsui, W.C. Oliver, G.M. Pharr, Influences of stress on the measurement of mechanical properties using nanoindentation: part I – experimental studies in an aluminum alloy, J. Mater. Res. 11 (1996) 752–759.
[45] A. Bolshakov, W.C. Oliver, G.M. Pharr, Influences of stress on the measurement of mechanical properties using nanoindentation: part II – finite element simulations, J. Mater. Res. 11 (1996) 760–768.
[46] N. Huber, J. Heerens, On the effect of a general residual stress state on indentation and hardness testing, Acta Mater. 56 (2008) 6205–6213.
[47] M.D. Mathew, G. Sasikala, K. Bhanu Sankara Rao, S.L. Mannan, Influence of carbon and nitrogen on the creep properties of type 316 stainless steel at 873 K, Mater. Sci. Eng. A 148 (1991) 253–260.
[48] C. Naudin, J. Frund, A. Pineau, Intergranular fracture stress and phosphorus grain boundary segregation of a Mn–Ni–Mo steel, Scr. Mater. 40 (1999) 1013–1019.
[49] R. Ding, A. Islam, S. Wu, J. Knott, Effect of phosphorus segregation on fracture properties of two quenched and tempered structural steels, Mater. Sci. Technol. 21 (2005) 467–475.
[50] H. Erhart, H.J. Grabke, Equilibrium segregation of phosphorus at grain boundaries of Fe-P, Fe-C-P, Fe-Cr-P, and Fe-Cr-C-P alloys, Metal Sci. 15 (1981) 401–408.
[51] M. Paju, H. Viefhaus, H. Grabke, Phosphorus segregation in austenite in Fe–P–C, Fe–P–B and Fe–P–C–B alloys, Steel Res. 59 (1988) 336–343.
[52] P. Sevc, J. Janovec, P. Lejcek, P. Záhumenský, J. Blach, Thermodynamics of phosphorus grain boundary segregation in 17Cr12Ni austenitic steel, Scr. Mater. 46 (2002) 7–12.
[53] A. Andrieu, A. Pineau, P. Joly, F. Roch, D. Ryckelynck, Influence of P and C intergranular segregation during manufacturing and ageing on the fracture toughness of nuclear pressure vessel steels, in: 20th European Conference on

Fracture (ECF 20), Jun 2014. Trondheim, Norway, 2014.
[54] M. Paju, R. Möller, The effect of boron on phosphorus segregation in austenite, Scr. Metall. 18 (1984) 813–815.
[55] H. Erhart, H.J. Grabke, Site competition in grain boundary segregation of phosphorus and nitrogen in iron, Scr. Metall. 15 (1981) 531–534.
[56] C. Briant, Nitrogen segregation to grain boundaries in austenitic stainless steel, Scr. Metall. 21 (1987) 71–74.
[57] C. Briant, P. Andresen, Grain boundary segregation in austenitic stainless steels and its effect on intergranular corrosion and stress corrosion cracking, Metall. Trans. A 19 (1988) 495–504.
[58] D. Argence, A. Pineau, Predictive metallurgy applied to creep-fatigue damage of austenitic stainless steels, in: The Donald McLean Symposium Structural Materials Engineering Application through Scientific Insight, 1995.
[59] M.W. Spindler, An improved method for calculation of creep damage during creepfatigue cycling, Mater. Sci. Technol. 23 (2007) 1461–1470.
[60] D. McLean, Grain Boundaries in Metals, Clarendon Press, 1957.
[61] T. Heyward, J. Goldstein, Ternary diffusion in the α and γ phases of the Fe–Ni–P system, Metall. Trans. 4 (1973) 2335–2342.
[62] H. Erhart, M. Paju, Phosphorus segregation in austenite, Scr. Mater. 17 (1983) 171–174.